Mapping Large Strains in Phase-Sensitive OCT: Key Role of Supra-Pixel Displacement Tracking in Incremental Strain Evaluation

Alexander A. Sovetsky, Alexander L. Matveyev, Lev A. Matveev, Grigory V. Gelikonov, and Vladimir Y. Zaitsev

Institute of Applied Physics Russian Academy of Sciences, 46 Ulyanova str., Nizhny Novgorod 603950, Russia

*** e-mail:** alex.sovetsky@mail.ru

Abstract. Displacement tracking is an important step in realization of compression optical coherence elastography (C-OCE), especially in the context of obtaining nonlinear stress-strain dependences and subsequent evaluation of the tissue Young's modulus. The rapidly progressing phase-sensitive C-OCE, however, enables direct measurements of only rather small interframe strains (below 1%), for which displacements are also small. Obtaining stress-strain curves for larger strains (~10% and greater) in phase-sensitive C-OCE can be made via cumulation of interframe strains and particle displacements. The resultant values of the so-found cumulative displacements may significantly exceed the pixel size, whereas measurements of the phase variations in C-OCE are usually performed by comparing the signals from the same pixel in a series of compared scans. When displacements of particles in a series of acquired scans reach supra-pixel values, simple pixel-to-pixel estimation of interframe phase variations may lead to significant errors in evaluating linear and nonlinear elastic properties of tissues. Thus, for large strains, adequate accounting for the resultant supra-pixel displacements of order of several pixels and greater is of key importance for undistorted mapping of elastic properties of heterogeneous materials, as well as for correct tracking of boundaries separating tissue regions with different elastic properties. In this paper we discuss the elastographic procedures of correct tracking of supra-pixel displacements in phase-sensitive C-OCE and give real examples demonstrating the importance of such displacement tracking for undistorted reconstruction of two-dimensional maps of linear and nonlinear elastic properties of real biological tissues.

Keywords: Optical coherence elastography; compression elastography; OCE; strain mapping; elasticity mapping.

Paper #3508 received 14 Jul 2022; revised manuscript received 15 Aug 2022; accepted for publication 21 Aug 2022; published online 22 Sep 2022. doi: 10.18287/JBPE22.08.030304.

1 Introduction

Visualization of deformations in optical coherence tomography has been attracting much attention since the seminal paper by J. Schmitt [1], in which of the idea of compression elastography [2] initially proposed in medical ultrasound was transferred to optical coherence elastography. As a result of intense effort of various groups working in Optical Coherence Elastography (OCE), a breakthrough in the development of OCT-based methods for mapping genuine local strains occurred in the recent ~5 years, so that practically operable realizations of OCT-based strain visualization, as well as stiffness mapping using the compression OCE principle were demonstrated [3–8]. Of key importance in realization of these methods was the development of the

phase-resolved approach to mapping axial strains. In particular, in Ref. [3] the least-square fitting for finding axial gradients of interframe phase variations was proposed with the additional amplitude weighting, due to which noisy contributions of small-amplitude pixels can be appreciably suppressed. Works [5, 6] proposed advanced variants of determining such gradients based on the vector approach (in which the complex-valued amplitudes are processed as vectors in the complex plane). The vector method also realizes amplitude weighting, obviates the necessity of conventionally required phase unwrapping for supra-wavelength displacements of scatterers and is especially tolerant to various measurement errors (including both the noises of the receiving array and deformation-induced decorrelation of the compared OCT scans). It should also be mentioned that in parallel with the above-mentioned approach to OCE realization, in which mapping local strains is of key importance, there is another approach, dynamic OCE methods which utilize measurements of elastic-wave velocities either for shear waves or surface waves (see, e.g. reviews [9, 10]). However, wave-induced perturbations usually have fairly small amplitude with essentially sub-pixel displacements and, furthermore, estimation of local strains is not required for their tracking. In view of this, the problem of mapping large strains and supra-pixel (of the order of several pixels and greater) displacements does not arise in dynamic OCE methods, but is important for compression OCE, in which, besides small-amplitude perturbations, nonlinearity of stress-strain dependences can be studied and the tissue strains may reach tens of percent [11]. It may also be noted that although the use of phase-sensitive OCT for mapping strains was proposed over 15 years ago [12, 13] in this study for estimating strains and presenting the corresponding experimental demonstrations we will use the vector method in form [6] for analyzing phase-sensitive OCT signals.

Like for other applications of phase variations (e.g. in the estimation of the Doppler phase shift) in what follows the discussion will be focused on the estimation of axial displacements u and axial strains $s = \partial u / \partial z$ related to the interframe variation Φ of the OCT signal as follows:

$$s = \frac{\lambda_0}{4\pi n} \frac{\partial \Phi}{\partial z}, \qquad (1)$$

where λ_0 is the central optical wavelength in vacuum and n is the refractive index.

For the straightforward comparison of phases in sequentially acquired phase-sensitive OCT scans, the maximal magnitudes of estimated strains and displacements are limited by decorrelation effects caused by both relative interframe displacements of scatterers and their displacements from one pixel of the reference OCT scan to a neighboring pixel in the other scan. For such supra-pixel interframe displacements direct pixel-to-pixel comparison of the current and initial phases leads to serious errors because for such strong displacements, the initial and current signal in the considered pixel is formed by essentially different scatterers that were initially located in neighboring pixels [4, 5]. However, if the interframe phase variation in the strained tissue does not yet experience phase wrapping within the vertical size of individual pixels, to a certain degree the decorrelation caused by vertical displacements of scatterers between the neighboring pixels can be compensated. This can be made by comparing phases of pixels with neighboring numbers in the compared scans instead of straightforward pixel-to-pixel comparison [4, 5]. In practice such compensation is fairly efficient for displacements about one pixel, but does not help much to improve the quality of phase-variation estimates if the interframe displacements are greater than one pixel. For "typical" OCT systems, the maximal interframe strains that can be directly estimated via pair-wise comparison of OCT scans roughly amount to ~1% [5].

However, larger strains that cause essentially supra-pixel displacements are also of great interest for various applications (e.g., for studying thermo-mechanical deformations, drying, osmotic deformations [14–19]), as well as for studying stress-strain dependences beyond the linear Hooke's law. The latter, for many tissues, may be essentially violated for strains on the order of several tens of percent [8, 20–22].

In such situations, even if estimation of fairly large deformations via direct pair-wise comparison of OCT scans is impossible, incremental approach can be applied by performing cumulation of smaller directly measurable strains for a sequence of OCT scans [23, 24]. This incremental approach makes it possible to quantify much larger deformations resulting in strains up to several tens of percent and multiple-pixel displacements.

Unlike small strains under such conditions even the notion of "correct" cumulative strain becomes dependent on the particular application of the estimated large deformations, so that different definitions of cumulative strain may be required for various tasks, for which procedures of estimating large cumulative strains also may require modifications. Indeed, different methods that are (nearly) equivalent for finding small strains may give strongly differing results for large cumulative strains and in some cases the inappropriately chosen method of finding cumulative strains may result in strongly erroneous conclusions.

In what follows we analyze the notion of cumulative strains and displacements, demonstrate situations in which one or another definition should be chosen, and formulate algorithms that give physically meaningful cumulative results depending on the particular task. In particular, we discuss correct finding of supra-pixel displacements including tracking of boundaries that are not contrasted in structural OCT scans, quantification of large strains, as well as quantification and visualization of elastic properties of elastically-nonlinear tissues, for which their stiffness pronouncedly depends of strain and stress, correct visualization of tissue nonlinearity and related issues. For experimental illustrations we will use OCT scans obtained with OCT systems operating at a

wavelength of 1300 nm (and spectral width 90–100 nm) similar to those used in previous works [22, 25, 26].

2 When displacement tracking is important for finding cumulative strains

The purpose of this section is to demonstrate that even if one is not interested in the displacements of the scattering particles themselves, but wants to estimate fairly large strains of the tissue, correct finding of these strains in most cases cannot be made without auxiliary estimation of displacements experienced by the scatterers. This is a fairly general statement except for a special case of spatially uniform strain distribution. Such a simple situation occurs when mechanically homogeneous tissue experiences spatially uniform uniaxial stress. In such a case the resultant strain is also spatially uniform. In practice uniaxial stress can be created in the vicinity of an output window of the OCT probe that compresses the tissue. It is assumed that the tissue is not confined in the lateral directions and can fairly freely expand laterally (this also implies that there is no appreciable stiction at the interface between the OCT probe and the tissue, which may be enabled by putting a lubricating liquid onto the tissue surface).

A corresponding real example is shown in Fig. 1 that demonstrates compression of a layer of homogeneous silicone compressed by the output OCT probe window under the control of an automated moving support enabling a constant compression rate. Fig. 1a shows a structural image in which the two rectangles 1 and 2 are located at different depths and show the initial positions of two processing windows over which the axial phase gradients $\partial\Phi / \partial z$ are estimated (and, therefore, strains can be found using Eq. (1)). Fig. 1b shows an example of the spatial distribution of the compression-produced interframe strain which, as expected, looks fairly uniform. The two rectangles 1’ and 2’ show slightly displaced positions of the scatterers initially located within windows 1 and 2. For the deeper rectangles 2 and 2’ the displacements are somewhat greater than for rectangles 1 and 1’. However, for small interframe displacements in Fig. 1b, it makes no sense to distinguish window 1 from 1’ and even the stronger displaced windows 2 from 2’. Fig. 1c shows the distribution of cumulative strain found via straightforward summation of interframe strains (for ~150 frames). The total variation in the silicone-layer thickness is over 30%, so that during the compression, the scatterers are gradually displaced outside the initial locations of the processing windows and are substituted by other scatterers. The position of particles initially located within window 1 by the end of compression shifts to position 1’ (so that still window 1 and 1’ are significantly overlapped), whereas window 2 shifts to the strongly displaced position labeled as 2’, so that window 2 and 2’ do not overlap at all and contain different portions of particles. However, since the “instantaneous” interframe strain is spatially uniform, for estimating strains, it makes no sense to track the actual positions of the same physical particles, so that processing windows with fixed coordinates enable correct estimation of strains. This statement is illustrated by the strain dependences shown in Fig. 1d obtained for the processing window 1, as well as for window 2 with the fixed position and gradually displaced window 2’. The procedure of tracking the gradual displacements of the particles is explained below in detail, however, Fig. 1 shows that, for the uniform silicone, such tracking does not affect the estimated cumulative strain. The cumulative strain in Fig. 1d for all three curves is found using straightforward summation of incremental interframe strains. In Section 3 another form of cumulative strain is discussed, but for illustration of the absence of changes in the result with/without window tracking in Fig. 1 the used straightforward summation is enough.

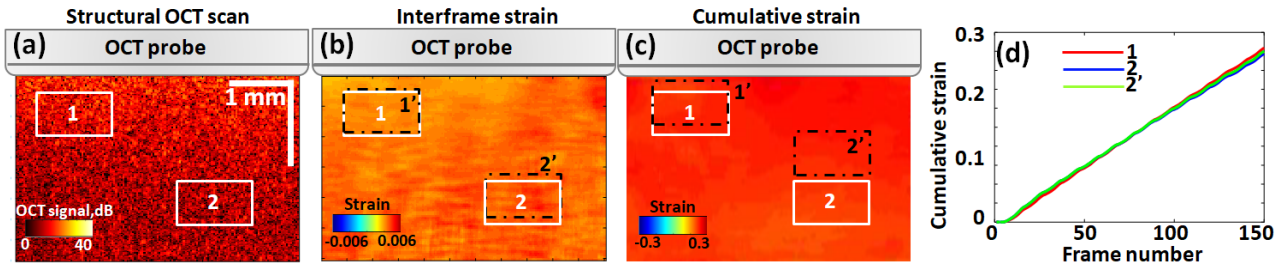

Fig. 1 Elucidation that in a homogeneous material correct strain can be found even without any displacement tracking. Panel (a) is a structural OCT scan of the compressed homogeneous silicone layer in which windows 1 and 2 with different vertical (lateral) coordinates are shown in the beginning of compression. Panel (b) shows the spatial distribution of interframe strain which is rather uniform over the entire visualized region (for the small interframe strains, the difference between initial posisions 1 and 2 and displaced positions 1’ and 2’ is insignificant). Panel (c) shows the much larger cumulative strain found by straightforward summation of interframe strains (notice than the deeper window 2 in the displaced position 2’ does not overlap with the initial position). Panel (d) shows the cumulative strain as a function of frame number found using the processing windows 1, 2 (without tracking) and 2’ with gradual tracking; all three curves are nearly indistinguishable even if for window 2’ the initial particles were substituted by new portions of the material.

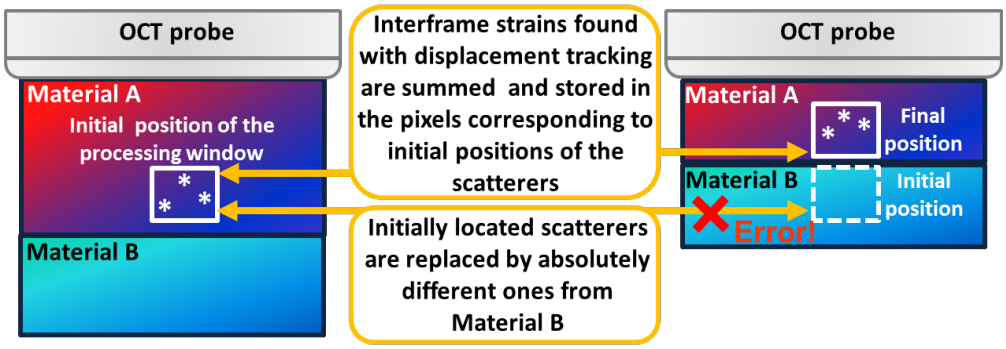

Fig. 2 The scheme explaining the importance of displacement tracking and the fallacy of finding local material strain in initial position of the processing window during the significant compression. It is clear that in the beginning of compression the window shown by the solid line contains a portion of Material A and by the end of compression it already contains only particles of Material B with a larger Young's modulus. Therefore, to correctly estimate strain for the portion of Material A (shown by asterisks) during the compression, one has to track the changed positions of this material portion and correspondingly shift the position of the window, over which the strain is found.

In contrast to the homogeneous sample shown in Fig. 1, usually real tissues are mechanically inhomogeneous. Consequently, during the material deformation, the same position of the processing window may correspond to different portions of the inhomogeneous material with potentially significantly different elastic properties and different deformability. It is known that deformability (stiffness) of different portions of inhomogeneous tissues may differ quite strongly (several times and greater, e.g. for cancerous and normal tissues [25–28]). Consequently, for a fixed coordinate, during deformation of heterogeneous tissues one tissue component can be substituted by the tissue portions with strongly different elastic properties. In view of this, to find the resultant (cumulative) strain for a particular portion of the tissue, the processing window should be gradually shifted to follow the displacement of a particular tissue portion. The necessity to track the displacement of the particles and correspondingly move the processing window for mechanically inhomogeneous samples, as well as the reason of possible errors when the particle tracking is not used, are schematically elucidated in Fig. 2.

The discussed displacement tracking is equivalent to continuous estimation of the thickness of the material layer separating the OCT window surface and the current position of the tissue portion that we aim to keep within the processing window. This tracking method should be operable for any point of the material even in the absence of any visible markers associated with the initial particular position of the window. Furthermore, for a mechanically inhomogeneous material, within the layer separating the OCT probe and the current position of the processing window, the strain distribution may be essentially non-uniform in space. To correctly estimate local strains for every tissue portion that gradually moves, one should synchronously move the processing window. In other words, one should know the current distance of each material portion from the OCT probe surface. In turn, in the absence of any trackable markers, to calculate the current distance for every tissue portion, one has to correctly estimate strain of each portion of the tissue within the layer separating the OCT probe surface and the processing window. Therefore, the tracking of the processing window position should be performed in a self-consistent manner: correct estimation of strains requires knowing of the current position (cumulative displacement) of each moving tissue portion, whereas tracking of the position of each tissue portion in the absence of trackable markers requires correct estimation of cumulative strains for all over-laying layers of the material.

It should be pointed out that small interframe (incremental) strains are unambiguously related by Eq. (1) with the axial gradient of interframe phase variations. We refer the readers to papers [3, 5, 6], where the estimation of this gradient was discussed in ample detail. Finding total (cumulative) strains and total strain-induced displacement of the scatterers was used in some earlier papers, e.g. [14, 16, 23]. However, those papers discussed fairly homogeneous tissues and moderately large strains (usually essentially below 10%), for which tracking of a particular tissue portion was not very critical in contrast to strongly heterogeneous tissues (such as cancerous ones discussed in Ref. [22]), for which the procedures of correct particle tracking deserve a special detailed discussion.

We emphasize once again that only in special simplified cases (fairly uniform materials like in Fig. 1) large strains may be correctly evaluated independently of displacements. However, for most real mechanically inhomogeneous tissues, strain estimation performed without simultaneous tracking of displaced tissue portions with different elastic properties leads to strong errors. This in turn may significantly distort the diagnostic conclusions based on the OCT-elastography data.

Next, it can be pointed out that, unlike straightforward estimation of small strains via Eq. (1), the larger cumulative strain can be defined in different forms depending on the particular problem.

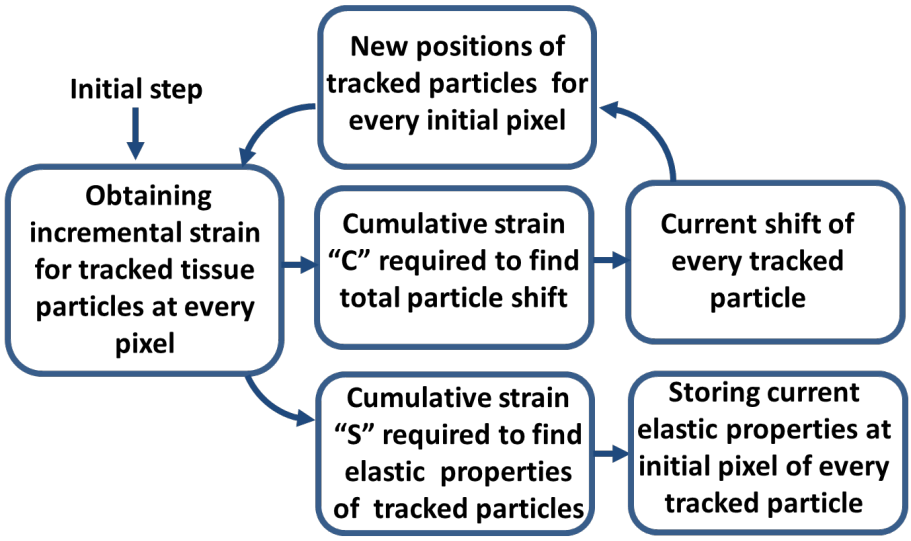

Fig. 3 Schematic of the self-consistent procedures of displacement tracking for correct evaluation of fairly large strains and accompanying variations in the elastic properties of the tissue. Namely, knowing the current distance between the OCT probe surface and every portions of the tissue is required to correctly evaluate strain of every tissue portion. In turn, knowing the current cumulative strains of all tissue portions is required to find the current position of every tissue particle (and to enable the corresponding shift of the processing window containing this tissue portion).

These definitions almost coincide for sufficiently small (say, ~ several %) strains, but significantly deviate for larger strains of the order of tens of percent. It can be shown that the "cumulative strain" destined for correct tracking of particle displacements the absence of evident markers (we denote this strain as "C") and cumulative strain intended for obtaining local "stress-strain" relationships and Young's modulus estimation (we denote it as "S") require different definitions.

In terms of notations "C" and "S" for the two definitions of cumulative strains the self-consistent procedures of strain estimation and displacement tracking are schematically depicted in Fig. 3.

In the following sections we explicitly give the definitions of cumulative strains "C" and "S", explain their inter-relations and present experimental examples to illustrate the importance of the self-consistent tracking of cumulative displacements and local strains of the displaced tissue particles.

3 How to relate interframe strains to cumulative strain that defines thickness variation

For non-infinitesimal deformation of inhomogeneous material, correct estimation of local strains requires that the processing window, over which the local strain is estimated, should contain the same portion of the material. To enable tracking of the same material portion, one has to estimate the current thickness of the material layer separating the OCT probe surface and the initial position of the processing window. Sufficiently small incremental displacements can be found via pixel-to-pixel comparison of the phase for a pair of sequential complex-valued OCT scans. Then the axial strain S defined by Eq. (1) can be found by estimating the axial gradient of this interframe phase variation (e.g., using the least-square approach [3] or vector method [6]). Let us consider a sufficiently thin (and therefore mechanically homogeneous) layer, for which the current thickness is h_{i-1} by the $(i-1)$ acquired frame. Then a small incremental strain s_i between i^{th} and $(i-1)^{\text{th}}$ frames causes the following small change in the layer thickness $h_i = h_{i-1}(1+s_i)$, so that the resultant thickness after a series of n incremental strains is

$$h_n = h_0 \prod_{i=1}^{n} (1+s_i), \tag{2}$$

where h_0 is the initial thickness. Assuming for simplicity that incremental strains are identical, $s_i = s$ one obtains

$$h_n = h_0(1+s)^n = h_0\left(1+ns+\frac{n(n-1)}{2!}s^2+ \right.$$
$$\left. +\frac{n(n-1)(n-2)}{3!}s^3+\ldots+s^n\right) \tag{3}$$

For sufficiently small term $ns \ll 1$ (in practice, on the order of a few percent), Eq. (3) reduces to

$$h_n \approx h_0(1+S), \tag{4}$$

where we denote $S = ns$. In the general case, when incremental strains s_i are not necessarily identical, the definition of cumulative strain S found via

straightforward summation of incremental strains can be generalized as

$$S = \sum_i s_i. \tag{5}$$

However, if the condition $S \ll 1$ is not satisfied, Eq. (4) for the current thickness gives an appreciable error. For the exact estimation of the thickness variation, another definition of cumulative strain may be formulated (we denote this quantity as C)

$$h = h_0(1+C), \text{ or } \Delta h \equiv h - h_0 = h_0 C. \tag{6}$$

From comparison of Eq. (6) and Eq. (3) it is clear that in the case of identical incremental strains s,

$$C_n = ns + \frac{n(n-1)}{2!}s^2 + \\ + \frac{n(n-1)(n-2)}{3!}s^3 + \ldots + s^n. \tag{7}$$

In more general situations, when incremental interframe strains s_i are not necessarily identical, a convenient recurrent definition of C_n can be formulated:

$$C_{n+1} = C_n + (C_n + 1)s_n. \tag{8}$$

It should be recalled that for a mechanically inhomogeneous sample, to find the variation in the thickness of the entire layer separating the OCT-probe window and the tracked portion of the material, one should take into account the inhomogeneity of overlaying material. Schematically this is shown in Fig. 4 for a 3-layer case. In the general case the inhomogeneity is *a priori* unknown, so that the cumulative strain should be found for every pixel above the considered pixel J, such that the variation $\Delta H_n(J)$ in the total thickens of the overlaying material after n incremental steps of straining is given by

$$\Delta H_n(J) = H_{px} \sum_{i=1}^{J} C_n(J), \tag{9}$$

where H_{px} is the vertical pixel size. The depth of each processing window centered around a given pixel should be shifted by one pixel every time when the so-found additional displacement ΔH of the tracked portion of the material increases by H_{px} as shown in Fig. 4.

In the conclusion of this section we note that one can obtain another useful relationship between the cumulative strain C defined via the non-infinitesimal change in the thickness of a considered material layer (Eqs. (6) and (8)) and strains S found via straightforward summation of incremental strains s_i (see Eq. (5)). Using Eq. (5) and recalling that an arbitrary S can be represented as a sum of a large number p of infinitesimal identical incremental strains ($S = p \cdot s$, $s \ll 1$), Eq. (3) can be rewritten as

$$h = h_0 \lim_{p\to\infty}(1+s)^p = \\ = h_0 \lim_{p\to\infty}\left(1+\frac{S}{p}\right)^p = h_0 \exp(S). \tag{10}$$

Comparison of Eq. (10) and Eq. (6) indicates that the cumulative strains C and S are related as

$$C = \exp(S) - 1 \text{ and } S = \ln(1+C). \tag{11}$$

For sufficiently small deformations (in practice, below ~10%) both definitions of cumulative strains are almost indistinguishable, $S \approx C$, whereas for several tens of percent, cumulative strains S and C differ rather

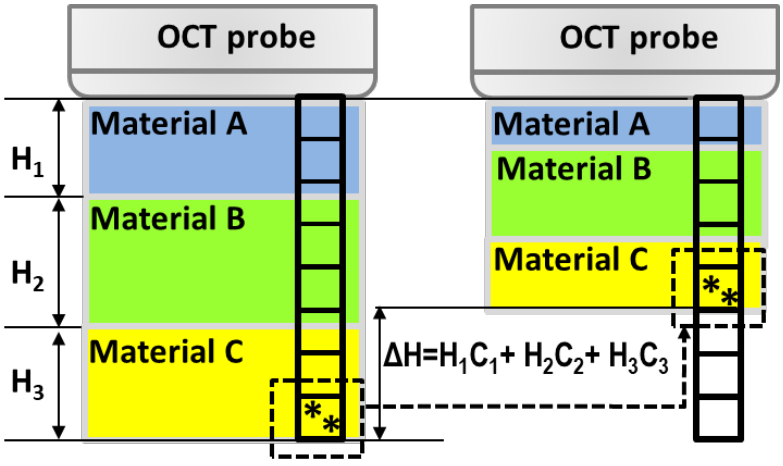

Fig. 4 Schematic of updating the processing window depth by estimating the deformation-produced displacement of tracked material portions.

significantly. Generally speaking, both strains S or C may be either positive or negative, their sign determines which one is greater in the absolute value. For compression (when S and C both are negative), $|C|<|S|$ and for expansion (when S and both are positive), $C > S$. As shown in what follows, the nonlinear relationship at Eq. (11) between S and C may be responsible for somewhat different conclusions about the material nonlinearity.

4 Usage of cumulative strains for obtaining nonlinear stress-strain relationships

In the optical coherence elastography based on the compression principle [1, 2] it was proposed to use the difference in strains of compressed layers for evaluation of differences in their Young's moduli. In the framework of the linear paradigm, for uniaxial stress σ created in the vicinity of the OCT probe that compresses the two layers of materials with the Young's moduli $E_{1,2}$, the resultant strains $s_{1,2} << 1$ produced by the same uniaxial strain σ are related via the linear Hooke's law:

$$\sigma = E_1 s_1 = E_2 s_2. \qquad (12)$$

For soft biological tissues, the linear approximation usually well holds for strains below 10^{-2}. In this case even if the applied stress is unknown, the relative value of the elastic moduli at different depths corresponds to the inverse ratio of the strains, $E_1 / E_2 = s_2 / s_1$. Thus, if for one layer its Young's modulus is known, the modulus for the second layer can readily be quantified. In practice, a layer of transparent or weakly scattering soft silicone with pre-calibrated Young's modulus can be placed over the examined tissue to enable quantification of its stiffness [7, 8] using the proportion (12).

The situation, however, is not that trivial if the created strains are not infinitesimal and, especially, if the constitutive equations $\sigma(s)$ relating strains in the material and the applied stress are nonlinear. In what follows we discuss how this nonlinearity can be characterized in a wide range of strains up to several tens of percent, for which the definition of what is "correct" strain is less evident.

For an optically transparent silicone layer (like used in Ref. [7]), it looks natural to define its finite axial strain s_{finit} via the variation of the layer thickness:

$$s_{finit} = (h - h_0) / h_0 = \Delta h / h_0. \qquad (13)$$

Such a definition indeed was used in the compression OCE variant described in paper [7], where the strain in the bulk of the transparent reference layer was not measurable and only the total layer thickness could be estimated by tracking its boundaries. In terms of the above-introduced cumulative strains C and strain S, it is clear from Eq. (13) that in Ref. [7] the strain of the reference silicone layer was actually understood as strain C defined by Eq. (6).

As was mentioned in the discussion of Eq. (11), for strains on the order of several percent there is almost no difference between the cumulative strain C describing the variations in material thickness and strain S defined as straightforward summation of incremental small strains. However, in quite realistic situations strains in either reference layer or the examined tissue may reach significantly larger values, on the order of several tens of percent. In such cases the following questions arise: (i) whether the reference silicone can still be considered as an elastically linear material for strains >20–30% and (ii) if a material behaves as linear-elastic one, which of the two types of cumulative strains C or S should be linearly proportional to the applied stress?

The above formulated questions can readily be verified experimentally since, for strains >20–30%, the quantities C and S should differ rather pronouncedly according to their nonlinear inter-relationship (12). If one assumes that the stress-strain relationship (12) should hold for the strain defined via Eq. (6) (i.e., via the layer-thickness variation as in paper [7]), then the following relationship should be expected

$$\sigma = EC = E \cdot (\Delta h / h_0), \qquad (14)$$

which can be verified experimentally.

Another understanding of the material linearity implies that the linear proportionality (12) holds for small increments in stress and strain, $\Delta\sigma = E\Delta s$ with invariable proportionality coefficient E in a fairly broad total strain range. Then it should be expected that the same proportionality holds for cumulative strain S defined via Eq. (5):

$$\sigma = ES. \qquad (15)$$

Which of Eqs. (14) or (15) is closer to reality can be verified experimentally. Furthermore, this verification can be performed even without the necessity of independent measurement of stresses/forces by auxiliary force cells. Such a "self-calibration" test requires measurements of only local strains. Namely, one may perform compression of a sandwich structure made of two silicone layers with sufficiently strongly (say 5–10 times) differing elastic moduli as illustrated in Fig. 5a. For such silicones that are strongly-contrasted in stiffness, the strains under compression are also strongly different, so that for the softer silicone, its strain may reach values of several tens of percent, whereas for the stiffer silicone, the strain may remain sufficiently small $S, C << 1$ (say within a few percent). For such small strains, the two definitions of cumulative strains practically do not differ, $S \approx C$, and one should expect the small strain developed in the stiffer are proportional to the applied stress with a high accuracy (although the proportionality coefficient may remain unknown). This value proportional to stress can be plotted against the

larger strains, either C or S, of the softer silicone layer. In such a way it is possible to verify which of the assumed forms of the Hooke's law (Eq. (14) for C or Eq. (15) for S) is closer to a linear dependence in a wide range of strains.

The results of such experimental verification are shown in Fig. 5b for two pair of silicones with the approximate proportions of the elastic moduli 550 kPa / 40 kPa and 550 kPa / 100 kPa. We emphasize, that precise values of the Young's moduli are not required for the verification of linearity. Fig. 5 demonstrates that the appreciable difference between the cumulative strains C or S become noticeable for strains > 0.2. The main conclusion is that it is strain S found via straightforward summation of incremental interframe strains, for which the proportionality between the small strain in the stiffer silicone (vertical axis) and larger strain S of the softer silicone (horizontal axis) remains nearly perfectly linear up to strains ~0.4–0.5. In contrast, for cumulative strains C the dependence is pronouncedly nonlinear starting from values ~0.2.

It is also interesting to mention that the stress-strain data presented in paper [7] demonstrate pronounced nonlinearity of the relationship between independently measured stress and strain C defined via variations in the silicone-layer thickness (see Eq. (14)). However, using the relation (11) between C and S, one can easily replot these data from [7] in the form $\sigma = \sigma(S)$. The two curves in the replotted form and original one from [7] are shown in Fig. 5c. It is clear that in the replotted form $\sigma = \sigma(S)$ data [7] look as a fairly linear dependence up to strains $S \sim 0.4 - 0.5$ similarly to the nearly-linear dependences shown in Fig. 5b for the same strain range.

For even larger strains, the additional stiffening of silicones becomes noticeable. It is likely, however, that this stiffening is mostly caused by adhesion/stiction effects. Indeed, the elastic response of a material is determined by the Young's modulus only for true uniaxial loading when the material is not confined in the lateral direction and can freely expand laterally. Stiction to either OCT probe glass or to the rigid bottom surface (or both) may significantly impede the lateral expansion, such that the material begins to experience some contribution of volumetric ("all-round") compression, the reaction to which is determined by the bulk modulus K rather than the Young's modulus $E<<K$. For biological tissues and similar materials (like soft silicones), this difference may reach 5–6 orders of magnitude, such that even incomplete stiction may cause noticeable coupling with the bulk compression, which may result in quite a significant difference between the true Young's modulus and its apparent higher value distorted by insufficiently free lateral expansion of the material due to stiction to the contacting rigid surfaces. Very clearly this influence of stiction on the apparent increase in the Young's modulus can be seen using weakly scattering silicone layers, in which the local depth-resolved strains can be readily visualized in the silicone bulk (experimental examples of such apparent stiffening due to stiction at the silicone-glass interface are shown in Ref. [8]). In practical measurements, putting lubrication (e.g. physiological saline solution) can be sufficient to significantly reduce the distorting role of stiction.

The above-presented considerations indicate that it makes no sense to state that one of cumulative strains C or S is "correct", because they reflect essentially different properties of the deformation process and both may be useful for different purposes.

For instance, for fairly large strains, when different material portions experience significant supra-pixel displacements, the varying positions of the tissue particles should be tracked as depicted in Fig. 3, which requires calculation of cumulative strains C to estimate the current thickness of the tissue layer separating every material particle and the OCT-probe surface.

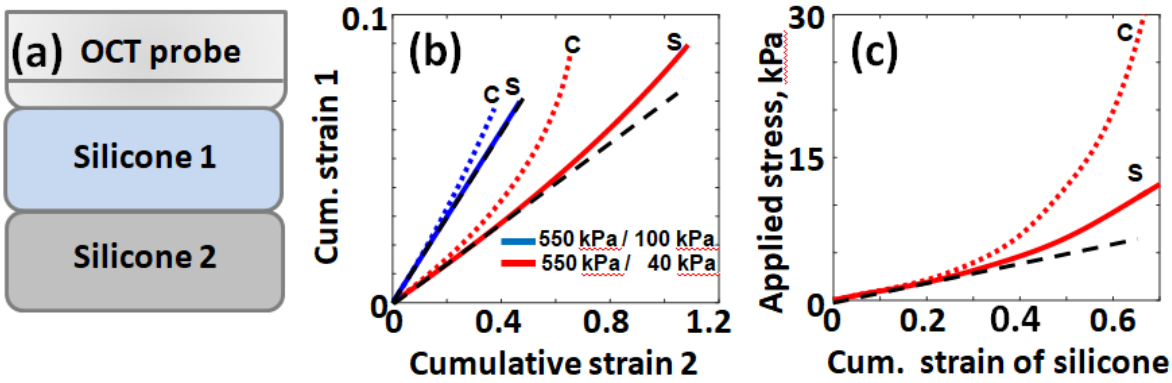

Fig. 5 Verification of linearity of stress-strain dependences for silicones. (a) is the scheme of the "self-calibration test" based on compression of two layers with strongly contrasting stiffness, so that sufficiently small strain ($S \approx C < 0.1$) in the stiffer silicone is linearly proportional to stress with a good accuracy. In plot (b) the vertical axis is for the smaller strain $S \approx C < 0.1$ of the stiffer silicone (proportional to stress with a good accuracy) and the horizontal axis corresponds to either C or S in the softer silicone. It is clear that for large strain $S \sim 0.4 - 0.5$, the dependences are nearly perfectly linear. For comparison, (c) shows the independent data from paper [7] for stress measured with a force cell and plotted as a function of cumulative strain C, as well as the same data recalculated as a function of strain S.

Next, if the goal is to verify linearity/nonlinearity of the elastic response for the tracked tissue portions, then cumulative strains S should be calculated for each tissue particle characterized by its initial depth and lateral coordinate. Thus, for characterization of nonlinear elastic response of tissues, it follows from the discussion of Fig. 5 that it is reasonable to plot the cumulative strain S in the reference silicone against strain S in the examined material with unknown elastic behavior. Due to the verified linearity, strain S in the pre-calibrated silicone readily allows one to quantify local axial stress for every lateral coordinate. For an elastically linear examined material (like another silicone), such a S -versus- S plot should be linear in the strain range up to 30–50%, although for further increase in strain, it is likely that adhesion/stiction influence may cause the deviation from the linear dependence even for a pair of ideally linear materials. For working with real biological tissues, such a strain range limited to 30–50% looks more than sufficient, because even for easily deformable tissues, usually strains should not exceed 10–20% to prevent irreversible mechanical damage. Furthermore, many tissues demonstrate pronounced elastic nonlinearity even for strains of the order of a few percent [8].

It should be emphasized that the sought nonlinear stress-strain dependences of real heterogeneous tissues should refer to every physical portion of the tissue rather that to every position in a fixed coordinate system. For strains on the order of several tens of percent, material particles may experience significant supra-pixel displacements, so that their tracking is critically important for obtaining the correct (undistorted) form the stress-strain curves for different components of real inhomogeneous tissues. The corresponding experimental examples demonstrating how these curves may be distorted without duly performed tracking are given in what follows.

5 How to visualize current elastic properties of the strongly deformed tissue

In the course of non-infinitesimal deformations, the tissue may pronouncedly change its form in the obtained series of images. Thus, tissue particles are characterized by different coordinates in different frames in the acquired series of images. In view of this, to enable comparison of the tissue properties for different stages of deformation, it is reasonable to ascribe the information about gradually-varying elastic properties of the tracked tissue particles by storing the current estimated elastic properties in the pixels corresponding to the initial coordinates of the particles. For the so-performed elastographic visualization, it is possible to clearly see how the elastic properties of every tissue portion are evolved, because in such a representation corresponding to the initial form of the tissue the geometrical form of tissue regions will remain invariable.

Before turning directly to the corresponding experimental examples, another important note should be made about visualization of the current (tangent) Young modulus. It is equal to the slope of the stress-strain curve $\Delta\sigma/\Delta S$, so that for tissues with nonlinear stress-strain dependences $\sigma(S)$ (like breast cancer sample discussed in Ref. [8]), the tangent Young's modulus strongly depends on the current stress (pressure). This pressure, however, in real conditions is usually rather non-uniform in the lateral direction over an OCT scan. The numerous reasons of this non-uniformity are incontrollable in practice [29]. In particular, the thickness of the reference silicone layer may fluctuate over the scan so that one region may already get in contact with the compressing OCT probe, whereas the other may be yet non-contacted; similarly the tissue surface often is pronouncedly non-planar; the tissue structure may be mechanically inhomogeneous laterally, so that the resultant strains for different coordinates may strongly differ even for the same stress value.

It is clear that in such situations utilization of force cells enabling the estimation of the average stress over the OCT probe surface does not help much, because the stress over the visualized region may unpredictably differ up to several times. In configurations similar to that shown in Fig. 6a, high linearity of silicones described by Eq. (15) makes it possible to use the silicone layer as a distributed fully-optical stress sensor [29]. When non-infinitesimal strains are of interest as discussed above, a series of OCT images are acquired and cumulative strains S and C are calculated using the above-described procedures with parallel displacement tracking. The current stress and strains of various tissue portions are attributed to their initial coordinates. Examples of such laterally inhomogeneous strain maps for various degrees of compression are shown in Fig. 6b. Having a series of such cumulative-strain maps, for every lateral coordinate (i.e., every A-scan) it is possible to find the frame number corresponding to a chosen stress value determined by the strain S in the pre-calibrated reference silicone (see Eq. (15)). Then the so-found A-scans with the desired stress level from strain maps with different numbers can be reassembled in a synthetic strain map, for which the stress is equal to the same pre-chosen value at every lateral coordinate. Such reassembled strain maps with the "standardized" stress over the entire scan are shown in the right part of Fig. 6b. This standardization allows one to estimate the current Young's modulus as the slope of the chord connecting the points with the pre-chosen stresses and corresponding strains as shown in Fig. 6b. In such a way maps of the Young's modulus for chosen standardized stresses can be readily plotted (see details in Ref. [29]). This procedure leads to the repeatability of the results, the possibility of comparing the stiffness both along one scan and among different scans and samples.

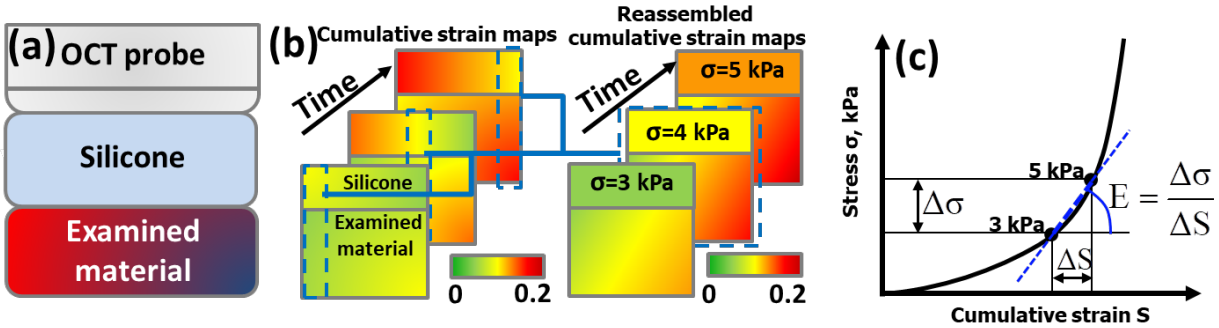

Fig. 6 Schematic of the OCE realization with silicone layers serving as optical stress sensors (a). A series of OCT scans obtains during compression of the tissue trough a silicone layer, in which its spatially-resolve cumulative strain S is linearly proportional to stress that may be laterally pronouncedly inhomogeneous as shown in the left part of panel (b). The right part of (b) shown a series of OCT scans with the same "standardized" pressure obtained by reassembling A-scans from the initially acquired OCT scans. Panel (c) shows an example of nonlinear stress-strain curve that can be obtained by plotting strain S in silicone proportional to stress according to Eq. (15) as a function of strain S in the studied tissue. After obtaining such spatially-resolved nonlinear curves, the Young's modulus of the tissue can be estimated for a chosen stress level.

Examples of application of these procedures to particular biomedical problems can be found in Refs. [22, 25] (morphological segmentation of human breast-cancer samples) and Ref. [26] (monitoring of morphological changes of animal-model tumors).

Using the experimental scheme depicted in Fig. 6, in the next section we discuss experimental examples demonstrating the key role of displacement tracking based on finding cumulative strain C, accompanied by finding cumulative strain S required for correct characterization of elastic properties of biological tissues.

6 Experimental examples demonstrating importance of self-consistent displacement and strain tracking for characterization of linear and nonlinear elastic properties of materials

The first example demonstrates strong influence of displacement tracking on the form of reconstructed stress-strain curves and the corresponding dependences of the tangent Young's modulus represented as a function of either current stress or strain of the tissue. For real nonlinear tissues, the latter dependences may differ quite significantly. Fig. 7 shows an example obtained for an excised rat cornea subjected to compression between two layers of soft reference silicone (with the Young's modulus $E = 50$ kPa). The experimental configuration is shown in Fig. 7a, where additionally a heating beam of IR laser is shown (because the experiments were made in the context of studies of new technologies of laser-assisted modification of microstructure and shape of collagenous tissues, which are in more detail discussed in Refs. [16, 30, 31]). The inhomogeneity of elastic properties of the corneal sample is related to the preliminary performed spatially-inhomogeneous moderate heating.

The structural images in the very beginning and at the end of the corneal sample compression are shown in Figs. 7b and 7c (notice that before compression the lower layer of silicone is not yet visible within the visualized depth). The initial position of the processing window is shown in Fig. 7b and its new position by the end of compression (tracked according to scheme shown in Fig. 2) is shown in Fig. 7c. In Fig. 7e the solid line shows the stress-strain curve found with correct tracking and the dashed line is obtained without tracking, i.e., for a processing window fixed in its initial position. It is clear that by the end of compression, the corneal layer inside the initial position of the processing window is completely substituted by the underlying silicone layer, so that the dashed curve is strongly distorted. Figs. 7f and 7g show the current slopes of the stress-strain curves (Young's modulus) found for the curves shown in Fig. 7e as functions of strain of the corneal tissue (for the tissue portion corresponding to the initial position of the processing window) and the stress applied to the tissue, respectively. Fig. 7f and 7g additionally clearly demonstrate that physically meaningful results with displacement tracking are strongly distorted when displacement tracking is not performed. Also, there is a clear difference between the dependences of the Young's modulus on either strain or stress. This fact is due to pronounced nonlinearity of the stress-strain relationship for the corneal tissue.

Figs. 7d and 7h show the 2D maps of the so-found Young's modulus distribution found for the stress 2 kPa standardized over the scan area (i.e., in the beginning of compression) and for much higher stress 30 kPa by the end of compression, respectively. Details of stress standardization can be found in Ref. [29]. Very strong stiffening of the corneal tissue is clearly seen in Fig. 7h in comparison with Fig. 7d, which is in contrast with invariable Young's modulus of the silicone layer in the upper parts of Figs. 7d and 7h.

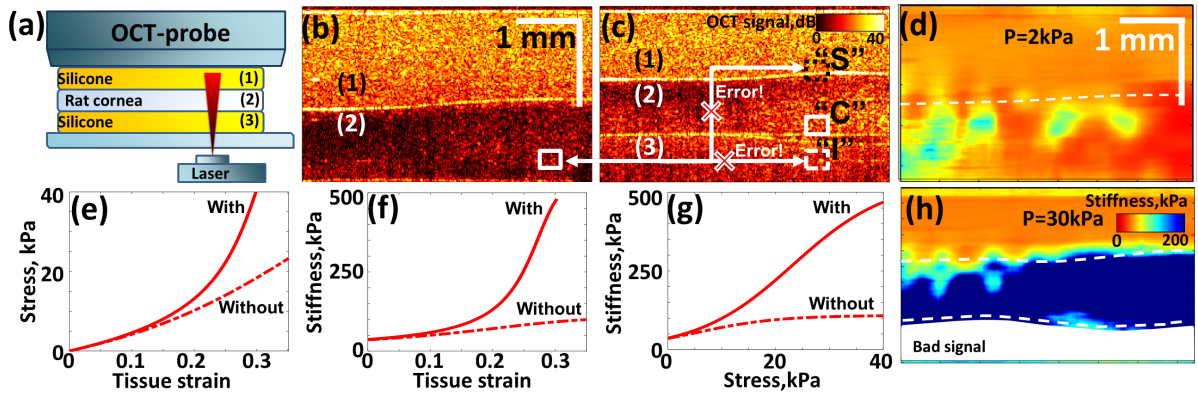

Fig. 7 Experimental demonstration of importance of displacements tracking for OCE examination of a strongly elastically nonlinear sample of rat cornea. Panel (a) illustrates experimental scheme of pore formation research based on stiffness changes of the rat cornea after laser exposure. Structural OCT images (b) and (c) corresponding to the beginning and end of compression clearly illustrate significant displacement of the scatterers. 2D plots (d) and (h) demonstrate changes in the shape, position and stiffness (with standardization of pressure by 2 kPa and 30 kPa) of the cornea in the beginning and by the end of compression. Panels (e), (f), and (g), for corneal particles in the irradiated zone, show stress-strain, stiffness-strain and stiffness-stress dependences in the correct and distorted forms found with and without displacement tracking, respectively. Index "I" in panel (c) denoted the initial position of the processing window (the same as in (b)) containing the tracked particles; index "C" shows the new position of the processing window containing the same tissue particles correctly found by calculating cumulative strain C, and index "S" shows erroneously found new position found using strain S instead of C. The dashed lines in (d) and (h) show the boundary between silicone and corneal tissue.

It can also be emphasized that the geometrical shape of the tissue in the OCT images may vary not only due to the mechanically created deformations, but may additionally be distorted by procedures of obtaining synthesized scans to enable stress standardization. Indeed, the physical stress distribution may be pronouncedly inhomogeneous, so that desired "standardized" stress at different lateral coordinates may be attained for scans with different numbers. Consequently, in the "standardized" scans, assembled using A-scans taken from initial scans with different numbers, the geometrical shape of the tissue in the resultant pressure-standardized images may differ from real geometrical shapes of the examined tissue. This gives an additional argument that, to better represent how strongly different tissue portions change their elastic properties for a certain applied stress, it is reasonable first to track gradually varying positions for every pixel, but then to place the estimated current elastic parameters for every tracked particle into the pixels corresponding to the initial positions of those particles rather than to their current positions.

Fig. 8 based on real measurements of deformed corneal sample (the same as in Fig. 7) demonstrates in another form the difference between cumulative strains S and C, as well as the influence of their usage on the resultant stiffness maps. We recall once again that it is strain C, which correctly characterizes the change in the thickness of the tissue layer according to Eqs. (6). For compressive strains, according to Eq. (11) $|C|<|S|$. The difference between S and C may be significant as is clearly seen from comparison of the displacement maps in Fig. 8, where panel (a) corresponds to cumulative strain C that gives correct estimates of particle displacements, whereas Fig. 8b shows for every tracked pixel cumulative strain S using which one may overestimate displacements by the end of compression. The structural image corresponding to the initial state of the corneal sample was shown in Fig. 7b, where the layer of linear silicone with $E = 40$ kPa is clearly seen above the nonlinear corneal tissue. Next, Fig. 8c shows the spatial distribution of the estimated Young's modulus by the end of compression (for the maximal stress 40 kPa). The estimated Young's modulus for every particle is stored in the pixels corresponding to the initial sample configuration. The back-shift in Fig. 8c in correctly made based on the estimated strain C shown in Fig. 8a. Since Fig. 8c is obtained using correct back-shift to the initial pixels, the so-obtained elasticity map clearly shows that the thickness of the uniform layer of silicone well corresponds to its thickness in the structural image in Fig. 7b. In contrast, in Fig. 8d the back-shift to initial positions was made incorrectly, using strain S shown in Fig. 7b. Cumulative strain S strongly overestimated displacements, such that because of the over-estimated back-shift, the uniform layer of silicone looks much thicker. Correspondingly, the overall stiffness distribution is strongly distorted. For the considered example with a clear boundary between the tissue and silicone (see structural scan in Fig. 7b), this inconsistency with Fig. 8d can be rather easily noticed. However, usually inside real tissues are no such high-contrast boundaries, so that it is not so simple to compare structural and derived elastographic images.

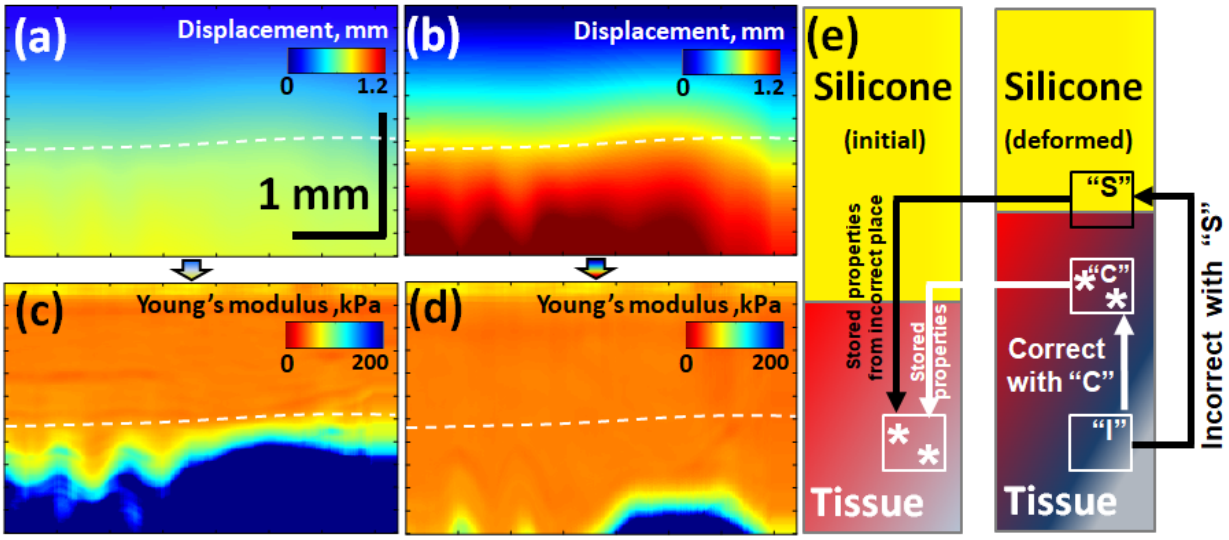

Fig. 8 Illustration of correct and incorrect displacement tracking (accumulated during gradual stress increase up to 40 kPa). Panel (a) is the correctly reconstructed displacement field based on the cumulative strain *C*; (b) is a similar incorrectly reconstructed displacement map based on utilization of cumulative strain *S*. (c) is the Young's modulus distribution obtained by correctly (d) is the Young's modulus map based on incorrectly back-shifted current position of every particle corresponding to panel (b) in which the displacement are over-estimated. Panel (e) schematically elucidates the reason of obtaining incorrectly back-shifted maps of elastic properties when the displacements are erroneously estimated using cumulative strain *S* instead of *C*. The dashed lines in panels (a)–(d) show the position of boundary between silicon and tissue as shown in the structural image in Fig. 6b.

Consequently, erroneously performed displacement tracking and back-shift of the current positions of particles may lead to strong distortions which are not easily detectable. Schematically the origin of the discussed errors in another form is elucidated in Fig. 8e, where correct (based on strain *C*) and overestimated (based on strain *S*) displacements and back-shifts are shown.

Fig. 8e demonstrates that when the displacement is significantly overestimated, one may erroneously place the current positions of tissue particles inside the layer of silicone and, consequently, to make too strong back-shift of the current positions of the tissue particles. Thus, the Young's modulus values actually found inside silicone can be erroneously ascribed to the tissue. When samples are mechanically depth-dependent and there are no evident layers/boundaries, the tracking of displacements can be based only on incremental estimations of strains, so that the proper method of finding cumulative strains is of key importance for correct displacement tracking.

Finally, it can be pointed out that the term "elastic properties" is not reduced to evaluation of the Young's modulus. Indeed, the described OCE method based on utilization of linear reference silicone layers enables obtaining nonlinear stress-strain dependences for examined tissues, from which not only the Young's modulus can be estimated (as elucidated in Fig 6c), but also dependences of the Young's modulus on either strain or applied stress can be derived as demonstrated in Figs. 7f and 7g. From the nonlinear stress-strain dependences and the derived pressure dependences of the Young's modulus one can estimate parameters of elastic nonlinearity of examined tissues. For example, one may use the following power-law expansion of the reconstructed stress-strain curves around a pre-selected stress σ_0:

$$\sigma = \sigma_0 + E(\sigma_0)\cdot(\varepsilon + \beta\varepsilon^2 + ...), \qquad (16)$$

where σ is the current stress, ε is strain, and σ_0 is the chosen initial stress around which the nonlinear stress-strain dependence is expanded; $E(\sigma_0)$ is the current (tangent) Young's modulus for $\sigma = \sigma_0$, and quantity β is the dimensionless nonlinearity parameter characterizing quadratic-in-strain nonlinearity.

By definition, the current Young's modulus corresponds to the slope of the stress-strain dependence (as illustrated in Fig. 6c), so that for the chosen pre-compression σ_0 one can write:

$$E(\sigma_0) = d\sigma / d\varepsilon\,|_{\sigma=\sigma_0}\,. \qquad (17)$$

As follows from Eq. (16), in the vicinity of point σ_0 the current Young's modulus can be represented as:

$$E(\sigma) = E(\sigma_0)\cdot(1 + 2\beta\varepsilon), \qquad (18)$$

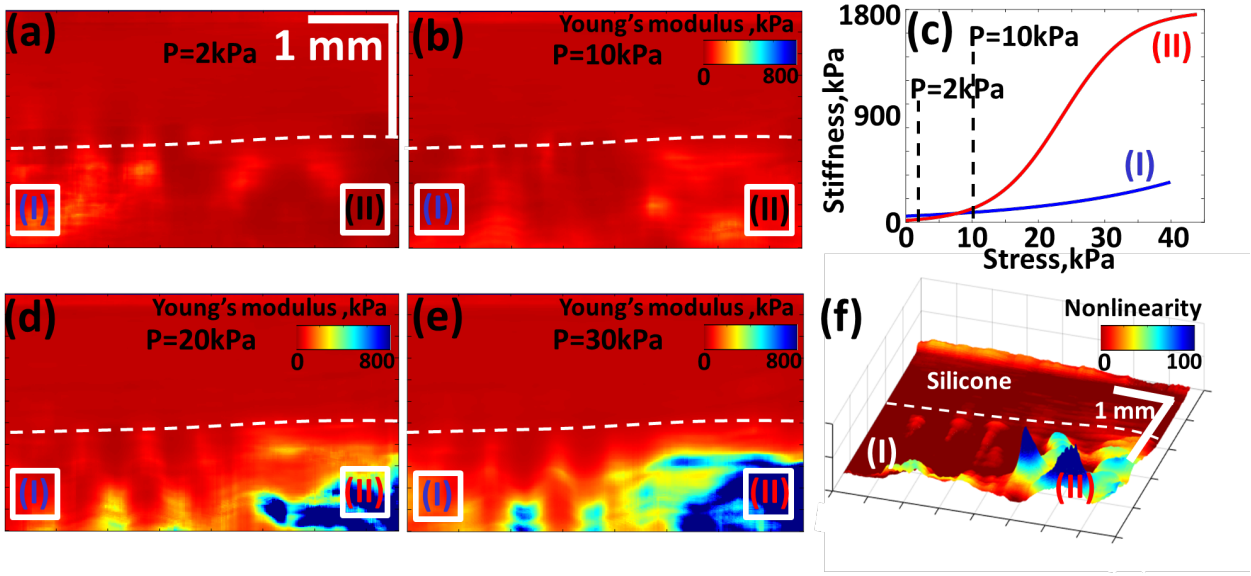

Fig. 9 Examples of the evolution of the Young's modulus maps with increasing stress and utilization of these maps for finding the nonlinearity parameter distribution. (a)–(e) Young's modulus maps for stresses 2 kPa, 15 kPa, 20 kPa, and 30 kPa, respectively. Panel (c) shows the stress-strain dependences for the regions (I) and (II) shown in panels (a)–(e). Panel (f) is the nonlinearity parameter distribution obtained by subtraction of the Young's modulus maps for 2 kPa and 10 kPa shown in panels (d) and (e).

so that the quadratic nonlinearity parameter β near the stress point σ_0 can be found as

$$\beta|_{\sigma=\sigma_0} = \frac{1}{2}\frac{dE}{E(\sigma_0)d\varepsilon} = \frac{1}{2}\frac{dE}{d\sigma}|_{\sigma=\sigma_0}. \qquad (19)$$

The initial stress $\sigma = \sigma_0$ can be chosen zero (corresponding to the very beginning of tissue compression) or some non-zero value may be chosen. Preliminary studies demonstrated that various tissue components (for example, morphological component of breast cancer) can exhibit very similar values of the Young's modulus, but at the same time the very same components may demonstrate clearly differing values of the nonlinear parameter β [22]. This fact opens the possibility to differentiate various tissue types using in combination the characteristic values of both the Young's modulus and the nonlinearity parameter.

In what follows for the same corneal sample that was used in Figs. 7 and 8, we demonstrate how the above described approach to mapping the current elastic properties of the tissue with the back-shift to the initial positions of the tissue particles can be used for convenient obtaining of the nonlinearity parameter. Indeed, it is clear that differential for of Eq. (19) can readily be represented in the difference form:

$$\beta|_{\sigma=\sigma_0} == \frac{1}{2}\frac{E(\sigma_0+\Delta\sigma)-E(\sigma_0)}{\Delta\sigma}|_{\sigma=\sigma_0}. \qquad (20)$$

Eq. (20) indicates that if one has the Young's modulus maps as in Fig. 8c obtained for fairly close stress levels σ_0 and $\sigma_0+\Delta\sigma$ with correct back-shift of the estimated local Young's moduli $E(\sigma_0)$ and $E(\sigma_0+\Delta\sigma)$ of the tracked tissue particles to the same initial pixels of the particles, then the pixel-to-pixel difference of such two maps $E(\sigma_0+\Delta\sigma)$–$E(\sigma_0)$ readily yields the map of the quantity $(1/2)\cdot\Delta\sigma\cdot\beta|_{\sigma=\sigma_0}$ proportional to the nonlinearity parameter.

Fig. 9 demonstrates the maps of the Young's modulus (similar to Fig. 8c) for four different levels of applied stress (2, 10, 20, and 30 kPa). The spatial inhomogeneity of the Young's modulus in the corneal sample is caused by spatially-inhomogeneous irradiation with the heating laser beam (see the scheme in Fig. 7a) prior to the elasticity measurements. The heating produces changes in the entire stress-strain curves, examples of which are shown in Fig. 9c for the regions labeled as (I) and (II). Finally, Fig. 9f shows the map of the nonlinearity parameter obtained by subtraction of the Young's modulus maps for 2 kPa and 10 kPa (Figs. 9a and 9b). Fig. 9f is represented in the pseudo-3D-form to clearer show the spatial inhomogeneity of the nonlinearity parameter. It is clear from Fig. 9c that in the stress range 2–10 kPa the Young's modulus values are fairly similar in regions (I) and (II), but the nonlinearity parameters are pronouncedly different as is clearly seen from Fig. 9f. Thus, combined consideration of both Young's modulus and nonlinearity parameter can be much more efficient for differentiation among various tissue types as demonstrated in Ref. [22] for breast cancer tissues.

We also emphasize that even if particles in the deformed material are gradually shifted with increasing pressure, the correctly-performed back-shift to the initial positions allows one to place the estimated elastic parameters to the invariable initial pixels of the particles. Due to this, for visualizing the nonlinearity-parameter

distribution, straightforward subtraction of the Young's modulus maps is sufficient.

7 Conclusions

In this paper we discuss the problem of correct tracking of particle displacement in compression optical coherence elastography. In the above consideration we focused on the axial displacements, although due to Poisson's effect axial compression also causes lateral strains and displacements. However, there are several factors due to which the effect of lateral displacements is of secondary importance compared with axial ones. Some of these factors relate to the OCT system and some other to the studied material and character of its deformation. First, from the viewpoint is signal analysis, the analyzed OCT signal phase is much stronger sensitive to axial scatterer displacements in comparison with lateral ones. Next, comparing displacements of tissue particles to neighboring pixels, it should be pointed out that the lateral size of pixels (in fact the diameter of a single axial A-scan) in conventional point-scanning OCT systems with weakly focused beams is several times greater than the vertical pixel size (the typical difference is 3–5 times). Another feature of scanning is that usually the A-scans are noticeably overlapped in the lateral direction (the typical overlap corresponds to another factor of 3–4 times). Thus, the neighboring A-scans visualize almost the same portion of the examined tissue. Comparing axial and lateral strains, it can be mentioned that for soft tissues with Poisson's ratio close to 0.5, lateral strains are twice smaller than the axial ones. Furthermore, for ideally plane-layered structures, in contrast to the depth dependence, the tissue properties do not depend on lateral positions at all, whereas the structure of many real biological tissues is close to plane-layered. Due to all these features, the elastographic images are at least an order of magnitude more tolerant to lateral motions.

By the above-mentioned reasons we focused on the problem of axial tracking in the context of estimation of larger strains and supra-pixel displacements, which has not specifically discussed in previous publications, although the interest to OCT-based phase-sensitive strain mapping and compression OCT-based elastography rapidly grows in the recent years in various research groups [7, 20, 32–34] (see also review [11] and Refs. therein). Obtaining of nonlinear stress-strain curves using compression OCT elastography opens previously unavailable prospects for high-selectivity differentiation of cancerous tissues [22]. For obtaining nonlinear stress-strain curves of real heterogeneous tissues in sufficiently broad strain ranges (say, for strains >10–20% that are still biologically non-destructive), the above-discussed tracking is of key importance. Without correctly performed displacement tracking one may obtain essentially erroneous maps of the reconstructed elastic parameters and, consequently, derive strongly incorrect diagnostic conclusions.

We demonstrated that even if direct measurements of such fairly strong interframe strains are prevented by strong decorrelation effects, correctly designed incremental procedures can be efficiently used to evaluate and map both linear and nonlinear elastic properties of examined tissues. For the discussed strain ranges up to several tens of percent, we considered various definitions of the notion of cumulative strain and elucidated which particular definition should be used for various applications/purposes. It was shown that incorrect choice of the definition may lead to essentially erroneous conclusions about the spatial distribution of the elastic properties and their nonlinearity. Although it this study we used a particular vector approach for phase-sensitive strain estimation, but generally speaking the procedures of self-consistent simultaneous tracking of large strains and displacements presented in Fig. 3 remain valid for other methods of incremental strain estimation (e.g., the least square phase-sensitive approach [3] or even amplitude-based correlational approaches if their accuracy can be made sufficient [35]).

The presented results construct the basis for rapidly developing biomedical diagnostic methods that are based on the utilization of differences in both linear and nonlinear elastic parameters of biological tissues, which is especially important for oncologic applications [22, 25–28].

Disclosures

The authors declare that they have no conflict of interest.

Acknowledgments

The study was supported by the Russian Science Foundation (Grant No. 22-12-00295).

References

1. J. Schmitt, "OCT elastography: imaging microscopic deformation and strain of tissue," Optics Express 3(6), 199–211 (1998).
2. J. Ophir, I. Cespedes, H. Ponnekanti, Y. Yazdi, and X. Li, "Elastography: A quantitative method for imaging the elasticity of biological tissues," Ultrasonic Imaging 13(2), 111–134 (1991).
3. B. F. Kennedy, S. H. Koh, R. A. McLaughlin, K. M. Kennedy, P. R. T. Munro, and D. D. Sampson, "Strain estimation in phase-sensitive optical coherence elastography," Biomedical Optics Express 3(8), 1865–79 (2012).

4. V. Y. Zaitsev, A. L. Matveyev, L. A. Matveev, G. V. Gelikonov, E. V. Gubarkova, N. D. Gladkova, and A. Vitkin, "Hybrid method of strain estimation in optical coherence elastography using combined sub-wavelength phase measurements and supra-pixel displacement tracking," Journal of Biophotonics 9(5), 499–509 (2016).
5. V. Y. Zaitsev, A. L. Matveyev, L. A. Matveev, G. V. Gelikonov, A. A. Sovetsky, and A. Vitkin, "Optimized phase gradient measurements and phase-amplitude interplay in optical coherence elastography," Journal of Biomedical Optics 21(11), 116005 (2016).
6. A. L. Matveyev, L. A. Matveev, A. A. Sovetsky, G. V. Gelikonov, A. A. Moiseev, and V. Y. Zaitsev, "Vector method for strain estimation in phase-sensitive optical coherence elastography," Laser Physics Letters 15(6), 065603 (2018).
7. K. M. Kennedy, L. Chin , R. A. McLaughlin, B. Latham, C. M. Saunders, D. D. Sampson, and B. F. Kennedy, "Quantitative micro-elastography: Imaging of tissue elasticity using compression optical coherence elastography," Scientific Reports 5, 15538 (2015).
8. V. Y. Zaitsev, A. L. Matveyev, L. A. Matveev, E. V. Gubarkova, A. A. Sovetsky, M. A. Sirotkina, G. V. Gelikonov, E. V. Zagaynova, N. D. Gladkova, and A. Vitkin, "Practical obstacles and their mitigation strategies in compressional optical coherence elastography of biological tissues," Journal of Innovative Optical Health Sciences 10(6), 1742006 (2017).
9. K. V. Larin, D. D. Sampson, "Optical coherence elastography–OCT at work in tissue biomechanics," Biomedical Optics Express 8(2), 1172–1202 (2017).
10. M. A.Kirby, I. Pelivanov, S. Song, Ł. Ambrozinski, S. J. Yoon, L. Gao, D. Li, T. T. Shen, R. K. Wang, and M. O'Donnell, "Optical coherence elastography in ophthalmology," Journal of Biomedical Optics 22(12), 121720 (2017).
11. V. Y. Zaitsev, A. L. Matveyev, L. A. Matveev, A. A. Sovetsky, M. S. Hepburn, A. Mowla, and B. F. Kennedy, "Strain and elasticity imaging in compression optical coherence elastography: The two-decade perspective and recent advances," Journal of Biophotonics 14(2), e202000257 (2021).
12. R. K. Wang, Z. Ma, and S. J. Kirkpatrick, "Tissue Doppler optical coherence elastography for real time strain rate and strain mapping of soft tissue," Applied Physics Letters 89(14), 144103 (2006).
13. R. K. Wang, S. J. Kirkpatrick, and M. T. Hinds, "Phase-sensitive optical coherence elastography for mapping tissue microstrains in real time," Applied Physics Letters 90(16), 164105 (2007).
14. V. Y. Zaitsev, A. L. Matveyev, L. A. Matveev, G. V. Gelikonov, A. I. Omelchenko, D. V. Shabanov, O. I. Baum, V. M. Svistushkin, and E. N. Sobol, "Optical coherence tomography for visualizing transient strains and measuring large deformations in laser-induced tissue reshaping," Laser Physics Letters 13(11), 115603 (2016).
15. H. Müller, L. Ptaszynski, K. Schlott, C. Debbeler, M. Bever, S. Koinzer, R. Birngruber, R. Brinkmann, and G. Hüttmann, "Imaging thermal expansion and retinal tissue changes during photocoagulation by high speed OCT," Biomedical Optics Express 3(5), 1025 (2012).
16. O. I. Baum, V. Y. Zaitsev, A. V. Yuzhakov, A. P. Sviridov, M. L. Novikova, A. L. Matveyev, L. A. Matveev, A. A. Sovetsky, and E. N. Sobol, "Interplay of temperature, thermal-stresses and strains in laser-assisted modification of collagenous tissues: speckle- contrast and OCT-based studies," Journal of Biophotonics 13(1), e201900199 (2019).
17. P. A. Shilyagin, L. A. Matveev, E. B. Kiseleva, A. A. Moiseev, V. Y. Zaitsev, A. A. Sovietsky, D. V. Shabanov, V. M. Gelikonov, K. S. Yashin, K. A. Achkasova, N. D. Gladkova, and G. V. Gelikonov, "Stabilization of the Scanning Pattern for Three-Dimensional Phase-Sensitive OCT Modalities: Angiography, Relaxography, and Monitoring of Slow Processes," Sovremennye Tehnologii v Medicine 11(2), 25 (2019).
18. S. Lawman, P. W. Madden, V. Romano, Y. Dong, S. Mason, B. M. Williams, S. B. Kaye, C. E. Willoughby, S. P. Harding, Y.-C. Shen, and Y. Zheng, "Deformation velocity imaging using optical coherence tomography and its applications to the cornea," Biomedical Optics Express 8(12), 5579–5593 (2017).
19. Y. Alexandrovskaya, O. Baum, A. Sovetsky, A. Matveyev, L. Matveev, E. Sobol, and V. Zaitsev, "Optical Coherence Elastography as a Tool for Studying Deformations in Biomaterials : Spatially-Resolved Osmotic Strain Dynamics in Cartilaginous Samples," Materials 15, 904 (2022).
20. T. A. Krouskop, T. M. Wheeler, F. Kallel, B. S. Garra, and T. Hall, "Elastic moduli of breast and prostate tissues under compression," Ultrasonic Imaging 20(4), 260–274 (1998).
21. Y. Qiu, F. R. Zaki, N. Chandra, S. A. Chester, and X. Liu, "Nonlinear characterization of elasticity using quantitative optical coherence elastography," Biomedical Optics Express 7(11), 4702 (2016).
22. E. V. Gubarkova, A. A. Sovetsky, L. A. Matveev, A. L. Matveyev, D. A. Vorontsov, A. A. Plekhanov, S. S. Kuznetsov, S. V. Gamayunov, A. Y. Vorontsov, M. A. Sirotkina, N. D. Gladkova, and V. Y. Zaitsev, "Nonlinear Elasticity Assessment with Optical Coherence Elastography for High-Selectivity Differentiation of Breast Cancer Tissues," Materials 15(9), 3308 (2022).
23. A. A. Sovetsky, A. L. Matveyev, L. A. Matveev, D. V. Shabanov, and V. Y. Zaitsev, "Manually-operated compressional optical coherence elastography with effective aperiodic averaging: Demonstrations for corneal and cartilaginous tissues," Laser Physics Letters 15(8), 085602 (2018).
24. Y. Bai, S. Cai, S. Xie, and B. Dong, "Adaptive incremental method for strain estimation in phase-sensitive optical coherence elastography," Optics Express 29(16), 25327–25336 (2021).

25. E. V. Gubarkova, A. A. Sovetsky, V. Y. Zaitsev, A. L. Matveyev, D. A. Vorontsov, M. A. Sirotkina, L. A. Matveev, A. A. Plekhanov, N. P. Pavlova, S. S. Kuznetsov, A. Y. Vorontsov, E. V. Zagaynova, and N. D. Gladkova, "OCT-elastography-based optical biopsy for breast cancer delineation and express assessment of morphological/molecular subtypes," Biomedical Optics Express 10(5), 2244 (2019).
26. A. A. Plekhanov, M. A. Sirotkina, A. A. Sovetsky, E. V. Gubarkova,S. S. Kuznetsov, A. L. Matveyev, L. A. Matveev, E. V. Zagaynova, N. D. Gladkova, and V. Y. Zaitsev, "Method for in vivo assessment of cancer tissue inhomogeneity and accurate histology-like morphological segmentation based on Optical Coherence Elastography", Scientific Reports 10(5), 2244–2263 (2019).
27. W. M. Allen, L. Chin, P. Wijesinghe, R. W. Kirk, B. Latham, D. D. Sampson, C. M. Saunders, and B. F. Kennedy, "Wide-field optical coherence micro-elastography for intraoperative assessment of human breast cancer margins," Biomedical Optics Express 7(10), 4139–4152 (2016).
28. L. Chin, B. Latham, C. M. Saunders, D. D. Sampson, and B. F. Kennedy, "Simplifying the assessment of human breast cancer by mapping a micro-scale heterogeneity index in optical coherence elastography," Journal of Biophotonics 10(5), 690–700 (2016).
29. A. A. Sovetsky, A. L. Matveyev, L. A. Matveev, E. V. Gubarkova, A. A. Plekhanov, M. A. Sirotkina, N. D. Gladkova, and V. Y. Zaitsev, "Full-optical method of local stress standardization to exclude nonlinearity-related ambiguity of elasticity estimation in compressional optical coherence elastography," Laser Physics Letters, 17(6), 065601 (2020).
30. V. Y. Zaitsev, A. L. Matveyev, L. A. Matveev, G. V. Gelikonov, O. I. Baum, A. I. Omelchenko, D. V. Shabanov, A. A. Sovetsky, A. V. Yuzhakov, A. A. Fedorov, V. I. Siplivy, A. V. Bolshunov, and E. N. Sobol, "Revealing structural modifications in thermomechanical reshaping of collagenous tissues using optical coherence elastography," Journal of Biophotonics 12(3), e201800250 (2019).
31. O. I. Baum, A. Yuzhakov, A. V. Bolshunov, V. I. Siplivyi, O. V. Khomchik, G. I. Zheltov, and E. Sobol, "New laser technologies in ophthalmology for normalisation of intraocular pressure and correction of refraction," Quantum Electronics 47(9), 860–866 (2017).
32. S. Kling, "Optical coherence elastography by ambient pressure modulation for high-resolution strain mapping applied to patterned cross-linking," Journal of the Royal Society, Interface 17(162), 20190786 (2020).
33. S. Kling, H. Khodadadi, and O. Goksel, "Optical Coherence Elastography-Based Corneal Strain Imaging During Low-Amplitude Intraocular Pressure Modulation," Frontiers in Bioengineering and Biotechnology 7, 453 (2020).
34. M. Singh, A. Nair, S. Aglyamov, and K. Larin, "Compression optical coherence micro-elastography of the cornea," Investigative Ophthalmology & Visual Science 62(8), 2033–2033 (2021).
35. V. Y. Zaitsev, A. L. Matveyev, L. A. Matveev, G. V. Gelikonov, V. M. Gelikonov, and A. Vitkin, "Deformation-induced speckle-pattern evolution and feasibility of correlational speckle tracking in optical coherence elastography," Journal of Biomedical Optics 20(7), 075006 (2015).